International Journal of Machine Tools and Manufacture 144 (2019) 103424

Contents lists available at ScienceDirect

International Journal of Machine Tools and Manufacture

journal homepage: www.elsevier.com/locate/ijmactool

Effects of a drawbar design and force on multipurpose aerostatic spindle dynamics

Dang Chi Cong[a,b], Jooho Hwang[a,b,*], Jongyoup Shim[b], Seung-Kook Ro[b], Tony Schmitz[c]

[a] Department of Nano-Mechatronics, University of Science and Technology, 217, Gajeong-ro, Yuseong-gu, Daejeon, 34113, Republic of Korea
[b] Department of Ultra-Precision Machines & Systems, Korea Institute of Machinery and Materials, 156, Gajeongbuk-Ro, Yuseong-Gu, Daejeon, 34103, Republic of Korea
[c] University of Tennessee, Mechanical, Aerospace and Biomedical Engineering Department, Knoxville, TN 37996, USA

ARTICLE INFO

Keywords:
Drawbar
Multiple-point receptance coupling
Tool point FRF
Contact parameters
Aerostatic bearing spindle

ABSTRACT

The tool point frequency response function (FRF), or receptance, is an important dynamic condition for machining processes, especially milling and finishing, as it enables users to calculate the most appropriate operating conditions, namely spindle speed and depth of cut, for achieving the best spindle performance. In this paper, we evaluate the effects of the drawbar on the tool point FRF of a multipurpose aerostatic spindle using a new procedure. The drawbar was considered to be nested inside the shaft and the receptance of the assembly was predicted based on a multiple-point receptance coupling approach. We coupled the tool holder and the tool to the receptance, so two types of contact parameter were considered simultaneously. We determined the contact parameters between the shaft and the tool holder, and between the tool holder and the tool, and included the values obtained when coupling with different combinations of tool holder and tool. We also evaluated the shaft-tool holder contact parameter for three different axial pulling forces. Moreover, we investigated the aerostatic bearing dynamics, including the stiffness and damping factor, in three different cases of supplied air pressure. Finally, we estimated the FRF of the tool under several aerostatic bearing and drawbar conditions and calculated stability lobe diagrams based on the estimated FRF. These results show that considering the drawbar improves the estimate of the tool point FRF and, subsequently, the stability lobe diagram. The effect of varying the length and density of the drawbar on the tool point FRF was also investigated.

1. Introduction

High-speed machining technology supports a wide range of industrial fields, including electronics, automotive, and aerospace. It improves the surface finish of a product as well as the machining accuracy by decreasing the cutting force applied as the cutting speed increases, especially in the case of very hard materials [1]. A key aspect of high-speed machining technology is the high-speed spindle, in particular, the high-speed spindle frequency response function, or FRF. Understanding the FRF of a spindle can prevent the spindle from running at critical speeds, provide higher stability during cutting, and avoid chatter through the use of stability lobe diagrams [2–5].

Aerostatic spindles are widely used to meet the increasing demand for fine finishing of surfaces by providing low friction for high-speed rotations. A drawbar is installed in the hollow spindle shaft of the automatic tool change (ATC) system of a multi-purpose spindle, e.g., the milling and finishing process only requires one spindle. Several researchers have investigated the effects of a drawbar on the dynamics of a spindle system [6,7] or presented a dynamics model of a spindle system [8], but they did not consider the tool holder or tool. Additionally, the contact parameters for the tool holder and spindle did not take rotation and moment into account [7]. Few researchers have studied the effects of a drawbar on the tool point FRF [9]. Neglecting the effects of a drawbar can have a detrimental effect on the estimation of the tool point FRF.

The tool point FRF can be obtained by taking measurements directly at the tool's free end using an impact test. However, the combination of tool and tool holder changes frequently during machining processes, and it is time consuming to apply this measurement method when there are large numbers of combinations of shaft, tool holder, and tool. Alternatively, the tool point FRF can be calculated analytically, using the well-known receptance coupling substructure analysis (RCSA) method proposed by Schmitz et al. [10,11]. The RCSA method has been generalized from a rigid to a non-rigid model to yield better estimates of

* Corresponding author. Department of Ultra-Precision Machines & Systems, Korea Institute of Machinery and Materials, 156, Gajeongbuk-Ro, Yuseong-Gu, Daejeon, 34103, Republic of Korea.
E-mail addresses: jooho@kimm.re.kr, jooho.hwang@gmail.com (J. Hwang).

https://doi.org/10.1016/j.ijmachtools.2019.103424
Received 10 April 2019; Received in revised form 12 June 2019; Accepted 14 June 2019
Available online 15 June 2019
0890-6955/

Nomenclature

$[G_{ii}]$	Assembly receptance matrix between output displacement/rotation at point i and input force/moment at point i
$[R_{ij}]$	Component receptance matrix between output displacement/rotation at point i and input force/moment at point j
$[K_{i\_j}]$	Contact parameter between substructure i and substructure j
$[K_{a1}]$,$[K_{a2}]$, $[K_{a3}]$, $[K_{a4}]$	Aerostatic bearing stiffness matrices
X_i, Θ_i	Transverse deflection [m] and rotation [rad] at point i
F_j, M_j	Force [N] and moment [Nm] at point j
H_{ij}	X_i/F_j receptance [m/N]
L_{ij}	X_i/M_j receptance [m/Nm]
N_{ij}	Θ_i/F_j receptance [rad/N]
P_{ij}	Θ_i/M_j receptance [rad/Nm]
q_j	Force vector including the force and moment acting on the drawbar at point j
U_{c1}	Generalized displacement/rotation vector on the shaft drawbar assembly at point c1
Q_{c1}	Generalized external force/moment vector acting on the shaft drawbar assembly at point c1

Subscripts

2b,3b	Point 2b, 3b implying that the air bearing has been included
c1,c2,c3,c4	Actual contact positions of the drawbar and the shaft, the air bearing has been included
2b′	Point 2b implying that the nut, collet, and tool inside the collet have not been included
3b′, c1′,c2′,c3′,c4′	Point 3b, c1, c2, c3, c4 implying that the air bearing has not been included
xf	Linear displacement-to-force relationship
xm	Linear displacement-to-moment relationship
θf	Rotation-to-force relationship
θm	Rotation-to-moment relationship

the FRF of a tool point by adding a contact parameter between the tool holder and the tool. Several researchers have studied how to evaluate this contact parameter [12,13], but did not take into account the effects of the drawbar. Researchers have proposed the model for predicting the tool holder FRF, but did not investigate the effect of the drawbar on the tool point FRF and tool holder end point FRF [14,15]. Typically, only the contact parameter between the tool and the tool holder was considered. The contact parameter between the shaft and the tool holder has been largely neglected, which could reduce the accuracy of tool point FRF estimation.

In this study, we investigated the effects of a drawbar on the tool point FRF. Firstly, we briefly describe the entire tool point FRF estimation process. Secondly, the contact parameters, including between the shaft and the tool holder, and the tool holder and various tool connections, as well as the aerostatic bearing dynamics were characterized experimentally. Both the stiffness and damping coefficients were estimated to improve the stability of the spindle prediction. Then, the tool point FRF was estimated using the RCSA method, including a coupling component that takes into account the two contact parameters, which we calculated based on the previously estimated bearing dynamics. Hence, we estimated the end point of the tool holder and the tool point FRF while taking into account the effects of a drawbar and different spindle conditions. We validated our estimates by applying our method to various tools and tool holders. Finally, we predicted the effect of various drawbar conditions on the tool point FRF.

2. Modeling for tool point dynamics of aerostatic spindle

An aerostatic spindle can be modeled as an assembly of several substructures, as shown in Fig. 1.

In the model shown in Fig. 1, Substructure I includes the flute and shank of the tool. Substructure II includes the tool-holder (i.e., the nut, collet, and tool shank for a collect connection). Substructure III includes the shaft, drawbar, and aerostatic bearings, with stiffness matrices $[\mathbf{K_{a1}}]$, $[\mathbf{K_{a2}}]$, $[\mathbf{K_{a3}}]$, and $[\mathbf{K_{a4}}]$. Note that the tapering component of the tool-holder is included in Substructure III. To estimate the dynamic response at the tool point, these three substructures were combined together with the aid of two contact parameters using the RCSA method. See Appendix A for background on the RCSA method.

A drawbar has a common neutral axis and is located inside a shaft. We used the four-point receptance coupling approach to describe the dynamic response of the combination of shaft and drawbar, as in Ref. [16]. These four points denoted as c1, c2, c3, c4 are the actual contact positions of the drawbar and the shaft; the structure is divided into three segments.

$$[G_{3b3b}] = \frac{U_{c1}}{Q_{c1}} = R_{c1c1}\frac{q_{c1}}{Q_{c1}} + R_{c1c2}\frac{q_{c2}}{Q_{c1}} + R_{c1c3}\frac{q_{c3}}{Q_{c1}} + R_{c1c4}\frac{q_{c4}}{Q_{c1}} \quad (1)$$

where $[G_{3b3b}]$ is the dynamic response of the assembly of Substructure III at point 3b. R_{c1j} is the generalized component receptance matrix, including the translational and rotational motion [17] of the drawbar. The subscript "j" represents one of four cases, namely c1, c2, c3 or c4. q_j is the force vector including the force and moment acting on the drawbar. U_{c1} and Q_{c1} are the corresponding generalized displacement/rotation and external force/moment vectors acting on the shaft drawbar assembly, as shown in Fig. 2. See Appendix B for details on the calculation of Equation (1). The direct receptance of the shaft is represented as a Timoshenko beam model with aerostatic bearing dynamics $[\mathbf{K_{a1}}]$, $[\mathbf{K_{a2}}]$, $[\mathbf{K_{a3}}]$, and $[\mathbf{K_{a4}}]$; these were evaluated experimentally. The receptance of the drawbar was modeled as a Timoshenko beam model (as shown in Fig. 3).

After taking into account the effects of the drawbar, we modeled the arbitrary tool-holder receptance (Substructure II) using Timoshenko beam theory, and then coupled it to the receptance of the shaft-drawbar assembly (Substructure III) using Equation (2):

$$[G_{2b2b}] = [R_{2b2b}] - [R_{2b3a}]([R_{3a3a}] + [G_{3b3b}] + [K_{3\_2}]^{-1})^{-1}[R_{3a2b}] \quad (2)$$

where [K3_2] is the contact parameter between Substructures III and II.

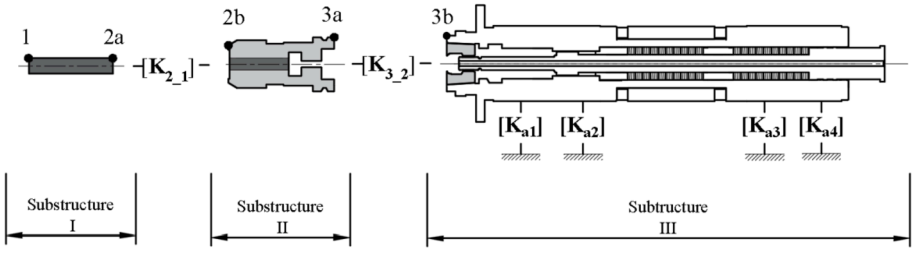

Fig. 1. Models combined into the substructure of a spindle.

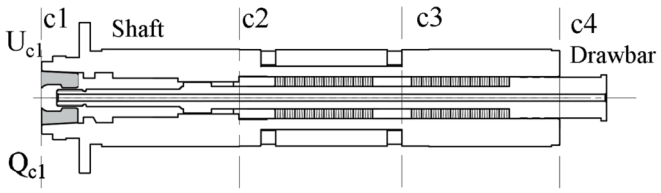

Fig. 2. Receptance coupling substructure analysis of the shaft and drawbar using the four-point receptance coupling approach.

We then estimated the receptance based on our experimental results and the known value of the tool holder receptance. These processes will be explained in more detail in the next section. The next step was to couple the tool (Substructure I) to the Substructure III-II assembly using Equation (3). The tool was modeled as a two-segment cylinder using Timoshenko beam theory. The parameter [K2_1] is the contact parameter between Substructures II and I; we estimated this value experimentally and used the known value of the receptance of a two-segment cylinder.

$$[G_{11}] = [R_{11}] - [R_{12a}]([R_{2a2a}] + [G_{2b2b}] + [K_{2\_1}]^{-1})^{-1}[R_{2a1}] \tag{3}$$

The two contact parameters [K_{3_2}] and [K_{2_1}] and the four dynamical quantities characterizing each of the aerostatic bearings are evaluated in the next sections.

2.1. Evaluation of contact parameter [K_{3_2}]

When modeling the free assembly of a spindle, as shown in Fig. 4, we require the receptance and contact parameter of the component so that we can estimate the receptance of the assembly using the RCSA method. Once the receptances of the component and assembly are known, we can calculate the contact parameter. Each time we evaluated the contact parameter in this paper, we used our experimental results to calculate the receptance of both the assembly and the individual components. This reduced the number of experiments required, in comparison to the method described in Ref. [9], where both the assembly and component receptances were estimated experimentally. The tool holder and the shaft, including the tool holder flanges forming Substructures II and III, respectively, were separated by a virtual section. The contact parameter [K_{3_2}] between Substructures III and II can be calculated by rearranging Equation (2) without considering the effects of the dynamics of the drawbar, as in Ref. [9], where one value of the contact parameter was chosen for each corresponding tool holder mode frequency from a set of contact parameters calculated using Equation (4) over the desired frequency range.

$$[K_{3\_2}]_{Previous} = (([R_{2b3a}]^{-1}([R_{2b2b}] - [G_{2b2b}])[R_{3a2b}]^{-1})^{-1} - [R_{3a3a}] - [R_{3b3b,S}])^{-1} \tag{4}$$

However, in reality the effect of the drawbar should also be taken into account. The contact parameter [K_{3_2}] can be calculated using Equation (5).

$$[K_{3\_2}] = (([R_{2b3a}]^{-1}([R_{2b2b}] - [G_{2b2b}])[R_{3a2b}]^{-1})^{-1} - [R_{3a3a}] - [G_{3b'3b'}])^{-1} \tag{5}$$

Equations (5) and (4) differ by the last term. In Equation (5), the term [$G_{3b'3b'}$] represents the rigid combination of the shaft and drawbar receptances. The effects of the aerostatic bearing dynamics are not taken into account when using this method to determine [K_{3_2}], which has the following form [12]:

$$[K_{3\_2}] = \begin{bmatrix} k_{xf} + i\omega c_{xf} & k_{xm} + i\omega c_{xm} \\ k_{\theta f} + i\omega c_{\theta f} & k_{\theta m} + i\omega c_{\theta m} \end{bmatrix} \tag{6}$$

where k and c represent the stiffness and damping parameters, respectively; ω is the frequency and i is the unit imaginary number. In Equation (6), subscripts xf, xm, θf, and θm indicate the linear displacement-to-force relationship, linear displacement-to-moment relationship, rotation-to-force relationship, and rotation-to-moment relationship between Substructures III and II, respectively. It is clear that once all of the terms on the left side of Equation (5) have been determined, the contact parameters between substructures III and I, i.e., [K_{3_2}] can be identified.

In Equation (5), the term [G_{2b2b}] is evaluated based on measured data at point 2b. Nevertheless, it is difficult to measure the term [G_{2b2b}] at point 2b in Fig. 1 because the tool, nut, and collet must be removed from Substructure II. In this paper, we use the superscript "′" in five cases, namely 3b′, c1′, c2′, c3′, c4′ and 2b'. The "′" in 3b′, c1′, c2′, c3′ and c4′ indicates that the air bearing has not been included. Meanwhile, the "′" in 2b′ indicates that the nut, collet, and tool inside the collet have not been included. Equation (5), which defines [K_{3_2}], should be amended to Equation (7), where the term [$G_{3b'3b'}$] is obtained by coupling the shaft and drawbar using the four-point receptance coupling approach, as in Equation (8). In Equation (7), four of the terms [$R_{2b'3a}$], [$R_{2b'2b'}$], [$R_{3a2b'}$], [R_{3a3a}] were obtained by applying the Timoshenko beam theory for the tool holder.

$$[K_{3\_2}] = (([R_{2b'3a}]^{-1}([R_{2b'2b'}] - [G_{2b'2b'}])[R_{3a2b'}]^{-1})^{-1} - [R_{3a3a}] - [G_{3b'3b'}])^{-1} \tag{7}$$

$$[G_{3b'3b'}] = \frac{U_{c1'}}{Q_{c1'}} = R_{c1'c1'}\frac{q_{c1'}}{Q_{c1'}} + R_{c1'c2'}\frac{q_{c2'}}{Q_{c1'}} + R_{c1'c3'}\frac{q_{c3'}}{Q_{c1'}} + R_{c1'c4'}\frac{q_{c4'}}{Q_{c1'}} \tag{8}$$

Up to now, we have not defined [$G_{2b'2b'}$] when evaluating [K_{3_2}] in Equation (7). This is the only term that has not been determined. In the following, we explain the term [$G_{2b'2b'}$], which is the receptance of the free-free combination at point 2b′ and has the form of Equation (9), from Ref. [18]. Furthermore, we reduced the noise in our calculations by applying this method to all of the FRFs measured:

$$[G_{2b'2b'}] = \begin{bmatrix} \frac{X_{2b'}}{F_{2b'}} & \frac{X_{2b'}}{M_{2b'}} \\ \frac{\Theta_{2b'}}{F_{2b'}} & \frac{\Theta_{2b'}}{M_{2b'}} \end{bmatrix} = \begin{bmatrix} H_{2b'2b'} & L_{2b'2b'} \\ N_{2b'2b'} & P_{2b'2b'} \end{bmatrix} \tag{9}$$

where $X_{2b'}$ and $\Theta_{2b'}$ are the transverse deflection and rotation at point 2b′, respectively; $F_{2b'}$ and $M_{2b'}$are the force and moment at point 2b′, respectively. $H_{2b'2b'}$ is the experimentally measured receptance, which we obtained from the results of an impact test and then used to synthesize [$G_{2b'2b'}$]. The experimental setup is shown in Fig. 4. In this experiment, the drawbar, shaft, and tool holder assembly were hung on an un-stretched cord. Theoretically, $H_{2b'2b'}$ is the ratio of the transverse displacement and force to the frequency. We recorded the acceleration

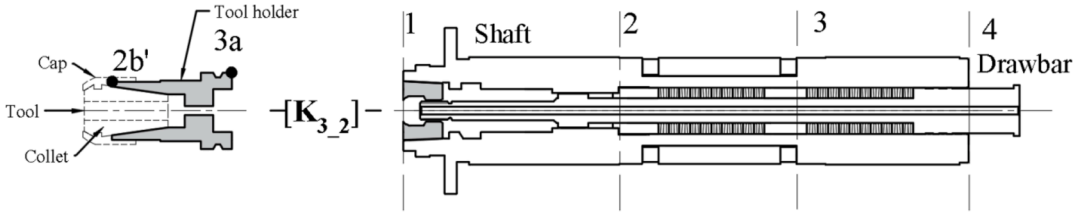

Fig. 3. Evaluation of the contact parameter [K_{3_2}] between Substructures III and II.

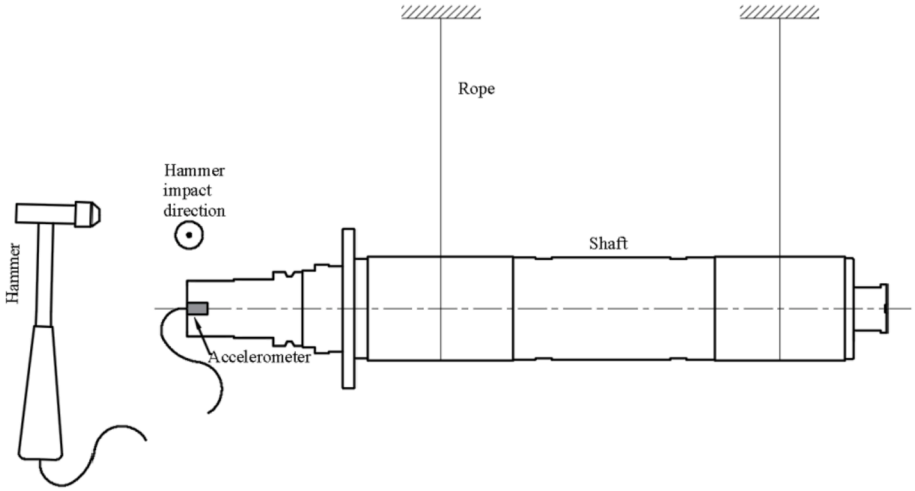

Fig. 4. Impact test setup for point 2b′ with shaft-drawbar-tool holder, approximating free-free boundary conditions.

$A_{2b'}$ (m/s^2) and hammer signal $F_{2b'}$ (N), which we then converted into the displacement per force ratio using Equation (10), as described in Ref. [18]:

$$[H_{2b'2b'}] = \frac{X_{2b'}}{F_{2b'}} = -\frac{1}{\omega^2}\frac{A_{2b'}}{F_{2b'}} \tag{10}$$

where $\omega = 2\pi f$ is the rotational frequency. After obtaining $H_{2b'2b'}$, three other receptances, including $L_{2b'2b'}$, $N_{2b'2b'}$, and $P_{2b'2b'}$, were evaluated based on the measurement of $H_{2b'2b'}$. By assuming that the measured data for $H_{2b'2b'}$ were obtained from a combination of M modes of a solid free-free Euler-Bernoulli beam, we were able to calculate three other receptances based on the characteristics of these modes. These characteristics include the beam diameter, d, beam length, L, solid damping factor, η, Young's modulus, E = 200 GPa, and density ρ = 7800 kg/m^3. While the Young's modulus and density were pre-defined; d and η were varied; L can be calculated using Equation (11) [19]:

$$L = \left(\frac{1.87510407^2 d}{2\pi f_n}\left(\frac{E}{16\rho}\right)^{1/2}\right)^{1/2} \tag{11}$$

Once these parameters have been defined, the response of the Euler-Bernoulli beam of all modes can be summed based on the measurement frequency bandwidth, which was calculated using $H^{cal}_{2b'2b'} = \sum_f \sum_{i=1..M} H^i_{2b'2b'}$. d, η, and L were adjusted using a optimization algorithm, in which we minimized the objective function PI (performance index), which represents the difference between the calculated value of $H^{cal}_{2b'2b'}$ and the measured value of $H^{meas}_{2b'2b'}$, which is the summation of the measured data, $H_{2b'2b'}$, in Equation (10), based on the frequency bandwidth, $H^{meas}_{2b'2b'} = \sum_f H_{2b'2b'}$. This method is based on the RCSA method for calculating the receptance presented in Ref. [20]:

$$PI = \sqrt{(\mathrm{Re}\,al(H^{meas}_{2b'2b'}) - \mathrm{Re}\,al(H^{cal}_{2b'2b'}))^2 + (\mathrm{Im}\,ag(H^{meas}_{2b'2b'}) - \mathrm{Im}\,ag(H^{cal}_{2b'2b'}))^2} \tag{12}$$

We obtained the values of the three parameters d, η, and L, by varying them until the calculated value of the receptance, $H_{2b'2b'}$, at point 2b′ agreed with measured data. These parameters were used to calculate $L_{2b'2b'}$, $N_{2b'2b'}$, $P_{2b'2b'}$ as in the Euler-Bernoulli beam approach presented in Ref. [20]. Having obtained $H_{2b'2b'}$, $L_{2b'2b'}$, $N_{2b'2b'}$, and $P_{2b'2b'}$, we were able to calculate $[G_{2b'2b'}]$. Hence, we evaluated $[K_{3\_2}]$ using Equation (7) and choosing the value of $[K_{3\_2}]$ for the most prominent tool holder frequency [9].

Although the results for $[K_{3\_2}]$ obtained using Equation (7) were based on the measured frequency bandwidth, we only used results for the tool holder modal frequency when evaluating the contact parameter dynamics representing the connections between Substructures III and II. The advantage of choosing the value of $[K_{3\_2}]$ at such a frequency is that it facilitates the FRF estimation in the tool holder modal frequency range, but the disadvantage is that this value of $[K_{3\_2}]$ is not suitable for other frequencies. This is due to unavoidable measurement errors. Therefore, the calculated value of $[K_{3\_2}]$ should be modified to make the calculated displacement-to-force receptance at 2b′ equal to the measured displacement-to-force receptance for a given frequency range rather than at the tool holder mode frequency only. We applied a fitting method to tune $[K_{3\_2}]$ until the value of $H_{2b'}$ calculated using Equation (7) fit the experimental data.

We also investigated the dependence of the axial force on the contact parameter. Adjusting the relative displacement of the drawbar and shaft using a screw mechanism affects the magnitude of the axial force induced by the spring disks of the drawbar, and thus changes the force acting on the spindle. We investigated three axial forces. In each case, we measured the tool holder end point 2b' and the receptance $H^{meas}_{2b'2b'}$, and calculated the contact parameter $[K_{3\_2}]$.

2.2. Identification of aerostatics dynamics

Once the contact parameter between Substructures II and III, $[K_{3\_2}]$, had been identified, we used the value to estimate the aerostatic bearing dynamics. When modeling a spindle with supplied air, the RCSA method requires three values, including the receptance of the component, contact parameter $[K_{3\_2}]$, and aerostatic bearing dynamics, to estimate the receptance of the assembly. Therefore, we were able to evaluate the aerostatic bearing dynamics once the other three values had been specified.

The aerostatic spindle used in this study contained four bearings, $[K_{a1}]$, $[K_{a2}]$, $[K_{a3}]$, and $[K_{a4}]$. We assumed that the individual bearings in the front and rear sets were equal, i.e., $[K_{a1}] = [K_{a2}]$, $[K_{a3}] = [K_{a4}]$. The aerostatic bearing dynamics $[K_a]$ can be written as [12]:

$$[K_a] = \begin{bmatrix} k_{xf} + i\omega c_{xf} & k_{xm} + i\omega c_{xm} \\ k_{\theta f} + i\omega c_{\theta f} & k_{\theta m} + i\omega c_{\theta m} \end{bmatrix} \tag{13}$$

In Equation (13), the aerostatic dynamics were assumed to have the same characteristics as the contact parameters $[K_{3\_2}]$. These include four types of stiffness, relating to the transverse displacement-to-force k_{xf}, displacement-to-moment k_{xm}, rotation-to-force $k_{\theta f}$, rotation-to-moment stiffness $k_{\theta m}$, and four types of damping, namely displacement-to-force c_{xf}, displacement-to-moment c_{xm}, rotation-to-force $c_{\theta f}$, and rotation-to-moment damping $c_{\theta m}$; ω is the frequency.

To identify the aerostatics of the bearing dynamics, we used the RCSA method to couple the receptances of the assembly at point 2b, the shaft and drawbar, and the tool holder. This process used the previously

evaluated contact parameter [K_{3_2}] to couple tool holder to the Substructure III. Substructure III was a combination of the aerostatic bearings, shaft, and drawbar, as shown in Fig. 1. The receptance of the spindle at point 2b is a function of four aerostatics bearing dynamics [K_a]. For each value of [K_a], the transverse displacement-to-force (k_{xf}) can be calculated using the Reynolds equation for a gas film in the bearing clearance. The governing equations for the gas film were solved using the finite difference method, based on parameters including the bearing clearance, feedhole diameter, and bearing diameter, etc. Other values in [K_a] were calculated by a further fitting process. In the front set of aerostatic bearings, the displacement-to-force stiffness was calculated as $k_{xf1} = k_{xf2} = 18 \times 10^6$ (N/m). In the rear set of aerostatic bearings, the displacement-to-force stiffness was calculated as $k_{xf3} = k_{xf4} = 16 \times 10^6$ (N/m). The dynamics of bearings (1) and (2) were assumed to be equal. We also determined the stiffness of each aerostatic bearing, k_{xf}, so seven parameters were left unidentified. Similarly, the values of seven other parameters were undefined for bearings (3) and (4). We added the bearing dynamics to the stiffness of the shaft at the intended bearing position. The receptance of the drawbar, defined by Equation (1), was evaluated to obtain [G_{3b3b}], and then coupled with the receptance of the tool holder to calculate [$G_{2b'2b'}$] using Equation (14), where [K_{3_2}] was determined in the previous section.

$$\left[G^{cal}_{2b'2b'}\right] = \left[R_{2b'2b'}\right] - \left[R_{2b'3a}\right]([R_{3a3a}] + [G_{3b3b}] + [K_{3\_2}]^{-1})^{-1}\left[R_{3a2b'}\right] \quad (14)$$

The nut, collet, and tool were considered to be point masses. The corresponding receptance (m/N) representing the summation of the masses of the nut, collet, and tool, m (kg), is $h_{2b2b} = -\frac{1}{m\omega^2}$, where ω is the frequency. This receptance was coupled to the receptance of the end point of the tool holder [$H_{2b'2b'}$] of [$G^{cal}_{2b'2b'}$] in Equation (14) by Equation (15).

$$[H^{cal}_{2b2b}] = [h_{2b2b}] - [h_{2b2b}]([h_{2b2b}] + [H_{2b'2b'}])^{-1}[h_{2b2b}] \quad (15)$$

[H^{cal}_{2b2b}] was used to fit the measured receptance at point 2b, [H^{meas}_{2b2b}]. After completing the fitting process, we obtained the aerostatic bearing dynamics [K_a]. We also evaluated [K_a] at various supplied air pressures. We used three values of the supplied air pressure, 0.4, 0.5, and 0.6 Mpa, to calculate [H^{meas}_{2b2b}] based on our experimental results, similarly to the calculation described Section 2.1. The setup for measuring [H^{meas}_{2b2b}] is shown in Fig. 6.

As shown in Fig. 6, we placed the spindle on foam to approximate free-free boundary conditions. The mode induced by the effect of the housing was removed from the measured data using a modal fitting process [21]. The purpose of this was to obtain agreement between the measured data and the model described in Fig. 5, where the effect of the housing was not included. We also removed the effect of the housing from the results of all of the other measurements described in this paper. The experiment setup to measure natural frequency (NF) of housing was similar to Fig. 6 except that the shaft was removed. The NF of housing was measured as 1771 Hz. This NF was close to second mode (1788 Hz) of spindle FRF as shown in Fig. 7. The effect of housing was considered as second mode of spindle FRF.

2.3. Identification of contact parameter [K_{2_1}]

Once [K_{3_2}] and the dynamics of the aerostatic bearings had been obtained, we used them to identify the contact parameter [K_{2_1}], which represents the contact between Substructures II and I. This was possible once the receptances of the components and assembly were known. We calculated [K_{2_1}] using Equation (16), which we obtained by rearranging Equation (3):

$$[K_{2\_1}] = (([R_{12a}]^{-1}([R_{11}] - [G_{11}])[R_{2a1}]^{-1})^{-1} - [R_{2a2a}] - [G_{2b2b}])^{-1} \quad (16)$$

We selected the results at the tool mode frequency to represent the connection between Substructures II and I. We used a tool blank rather than a real tool to determine the receptances [R_{12a}], [R_{11}], [R_{2a1}], and [R_{2a2a}] in Equation (16). The tool blank was cylinder-shaped and was made of the same material and had the same surface finish as the tool. Similar to the previous procedure for determining the receptance at the end of the tool holder, we measured the receptance at tool point H_{11} to evaluate G_{11} and calculated [H^{cal}_{2b2b}] based on the previous section, and then calculated [G_{2b2b}] using the RCSA method described in Ref. [20]. Again, this measurement should be carried out carefully to reduce noise, including the noise induced by the hitting point and the direction of the accelerometer.

3. Estimation of the FRF of the aerostatic bearing spindle

We now present our results for contact parameters [K_{3_2}], [K_{2_1}], and the aerostatic bearing [K_a]. We also discuss the applications of these results for different cases. The estimated FRF of the drawbar-shaft-tool holder assembly is described in Section 3.1. We then add the dynamics of the aerostatic bearings and estimate the resulting FRF in Section 3.2. Finally, we add the tool and estimate the total FRF in Section 3.3. We also investigated the effects of varying the length and density of the drawbar.

3.1. Tool holder end point FRF estimation

In the first stage, we coupled the drawbar and tool holder to the shaft. We used a different tool holder, tool holder B (17.5 mm collet length), to couple the components to verify the contact parameter [K_{3_2}], which we estimated using tool holder A (27.5 mm collet length). Tool holders A and B are shown in Fig. 8. The taper face and clamping conditions of all of the tool holders used in this study were the same.

The FRF at point 2b′ in the case with the drawbar was estimated in a similar manner to Equations (1) and (2), taking the dynamics of the aerostatic bearings into account; we did not include the nut, collet, or tool inside the cap. We measured the FRF at point 2b′ in the manner indicated in Fig. 4 and the results are shown in Fig. 9. The estimation of $H_{2b'}$ at the end point of tool holder A based on the contact parameter obtained with the drawbar was better than the estimate obtained when using the contact parameter calculated without taking the drawbar into account. The reason for this is that the receptance of the drawbar was included in that of the shaft when using the multipoint receptance approach. The estimated contact parameter [K_{3_2}] calculated using tool holder A was used to estimate the displacement-to-force receptance $H_{2b'}$ of tool holder B, and the results are shown in Fig. 10. The calculated values of K_{3_2} are shown in the first row of Table 1, where the axial pulling force of the tool holder clamping system was $F_z = 3.75 \times 10^3$ N. In the case without the drawbar, the NF (2464 Hz) deviated significantly from the measured value (2312 Hz) obtained in the case with the drawbar (2324 Hz), i.e., the accuracy of the estimation increased by 0.4%.

We also estimated the contact parameter under axial pulling forces, F_z, of 2.56×10^3 N and 1.17×10^3 N. The pulling force was measured using an axial force testing device, as shown in Fig. 11. Each time the pulling force was changed, the tool holder was re-clamped to the shaft, and then $H_{2b'}$ was estimated at the endpoint of the tool holder so that

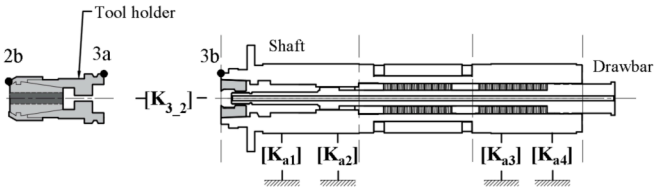

Fig. 5. Models of the spindle supported by aerostatic bearings using RCSA method.

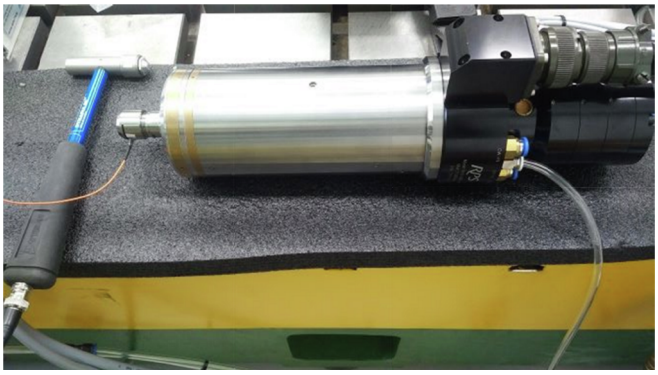

Fig. 6. Setup used to measure H_{2b2b} with various supplied air pressures, approximating free-free boundary conditions.

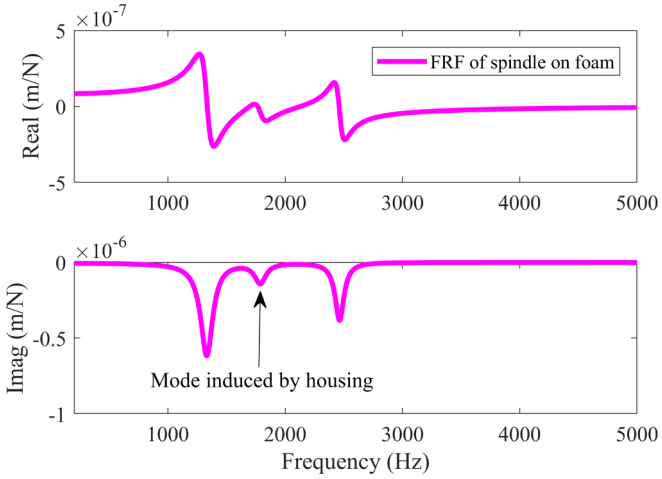

Fig. 7. Effect of mode induced by housing on FRF of spindle.

we could estimate the contact parameter under this clamping condition. The values of the contact parameters obtained under different clamping conditions are summarized in Table 1. These contact parameters were used in the next stage of the spindle modeling.

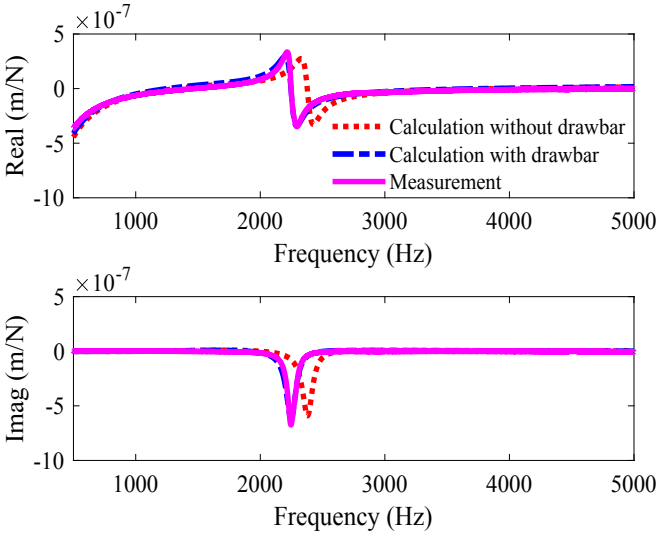

Fig. 9. Comparison between the calculated (without and with drawbar). and measured results for $H_{2b'}$ when using tool holder A.

3.2. Tool holder end point FRF of the aerostatic bearing spindle

In this section, we present the results of our analysis of the aerostatic bearings and our estimation of the tool holder end point FRF, taking into account the effect of the aerostatic bearings and drawbar. We estimated the results for the aerostatic bearings at air pressure 0.5 MPa in advance and used this estimate to predict the corresponding values at 0.4 and 0.6 MPa. The cases of 0.4 and 0.6 MPa were similar to the case at 0.5 MPa, as mentioned in Section 2.2.

We used the dynamical properties of the aerostatic bearings shown in Table 2 to estimate the receptance of the spindle at the end point of the tool holder, 2b', under different conditions. The data in Table 2 were estimated using tool holder A. For verification, we used these values to estimate the receptance of the end point of tool holder B, using Equations (1) and (2). We repeated these calculations for the case without the drawbar. The nut, collet, and tool inside the collet were not taken into account by these two calculations, so that we could maintain the configuration of the experiment in both cases. We carried out these measurements to compare the results with the calculated data, as

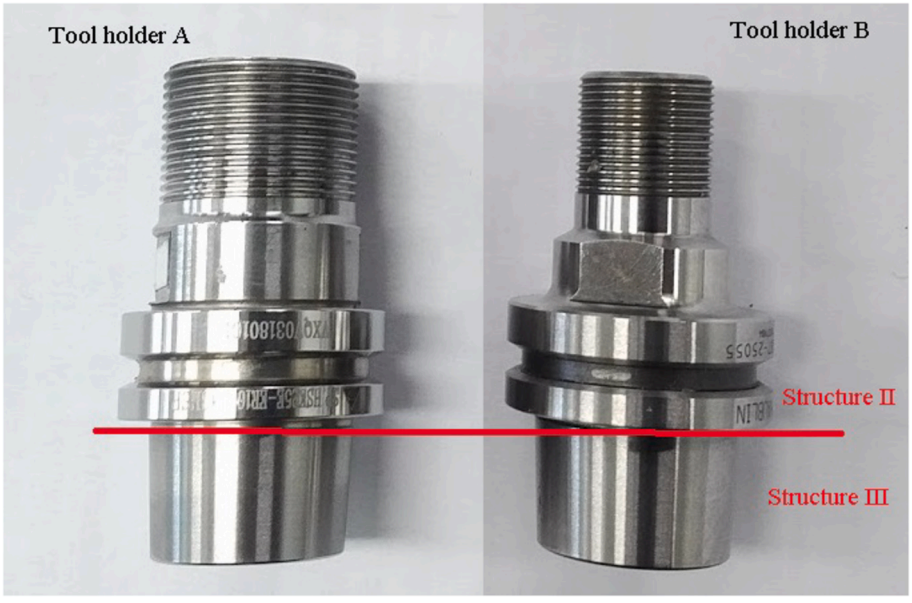

Fig. 8. Tool holders A and B.

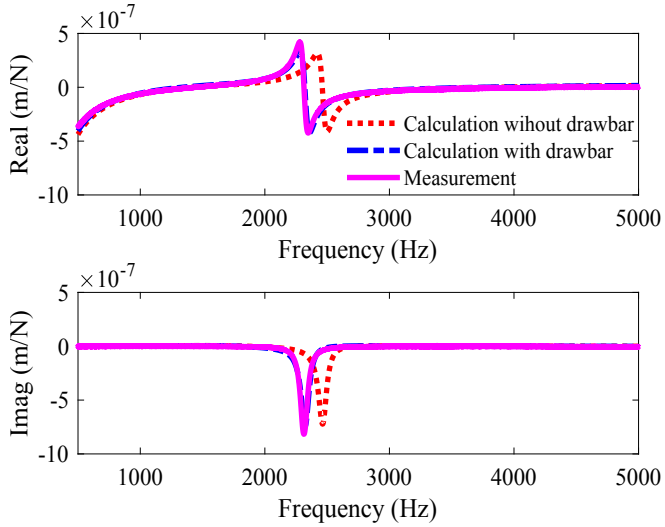

Fig. 10. Comparison between the calculated (with and without the drawbar). and measured FRF at point 2b′ using tool holder B.

shown in Fig. 12. In Fig. 12, the two NFs of the spindle are shown for the coupling between tool holder B and the shaft with an axial pulling force of 3.75×10^3 N. It is obvious that the calculation with the drawbar was more accurate than the calculation without the drawbar, due to the decrease in the NF induced by including the drawbar.

Fig. 13 shows the effects of the axial pulling force and the air pressure on the natural frequencies. The NF plane of tool holder A was lower than that of tool holder B due to A's larger size.

We then included the nut, collet, and tool inside the collet in our calculation. This enabled us to estimate H_{2b}, the FRF at point 2b. We calculated the full receptance $[G_{2b2b}]$ both with and without the drawbar. This calculation procedure was similar to the receptance calculation used in the RCSA method, which was described in Ref. [20] and summarized in Section 2.1. These receptance values, $[G_{2b2b}]$, were used in the next stage of our study.

3.3. Tool point FRF estimation and stability lobe diagram

The third stage of the coupling was to couple Substructure I to the spindle system using the estimated contact parameter $[K_{2\_1}]$ and a tool blank, as shown in Table 3.

We applied Equation (3) with the values of the contact parameters $[K_{2\_1}]$ and $[G_{2b2b}]$ and estimated the FRF of the tool point. We used tool holder A with d_s length of 27.5 mm for these calculations. In the measurement procedure, the blank tool was clamped to the tool holder of the spindle and the spindle was placed on foam, in a setup similar to that shown in Fig. 6. The results of the coupling calculations and measurements are shown in Fig. 14. We show the tool point FRF with a tool length of 32.5 mm on the left. We used this tool blank to estimate $[K_{2\_1}]$, and then repeated the estimation with a tool of length 42.5 mm, the results of which are shown on the right. Both carbide tools had a diameter of 6 mm. The estimation of the FRF was better when the drawbar was included than when it was omitted. This is because in the

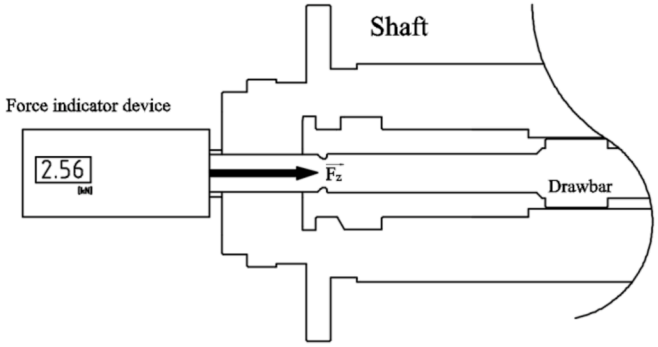

Fig. 11. Axial pulling force measurement.

previous coupling stage, the model without the drawbar provided a higher estimate in the second NF mode. Consequently, the NF of the tool without the drawbar was higher than that of the with-drawbar case. By including the drawbar in our model, we reduced the percentage error of in the tool mode NF to 1.3%, which is better than the 3.7% error obtained when the drawbar was not taken into account.

We estimated the stability lobe diagram (SLD) based on the FRF of the aerostatic spindle (Fig. 14) with the 42.5 mm tool blank clamped to tool holder A (Fig. 8). For the SLD calculation, the tool was assumed to have three flutes; the spindle to run clockwise; the milling type was set to face milling; the feed rate was 0.2 mm/flute; and the work piece was chosen as aluminum 7050-T7451. The SLDs of the FRF were calculated for three different cases and the results are shown in Fig. 15. We calculated the stability based on the FRF with the drawbar and found it to be much improved with respect to the depth of cut and spindle speed. These improvements did not only apply to low-speed operation (left) but were also observed in the case of high-speed operation (right), as shown in Fig. 15. For example, when the spindle ran at 19,500 rpm, as shown on the left in Fig. 15, the estimated SLD of the FRF without the drawbar implied that the spindle operation was stable until the depth of cut reached 1.8 mm. Meanwhile, the SLD of the FRF with the drawbar implied that the spindle operation was stable until the depth of cut reached 1.15 mm; this result is closer to the estimated SLD of the measured FRF (1.1 mm). Furthermore, for the lobe occurring at 17,000–30,000 rpm, the lowest depth of cut predicted by the FRF without the drawbar was 1.576 mm at 20,320 rpm; this is equivalent to a 42% error in the depth of cut for the measured FRF (1.104 mm) at 19,450 rpm. Meanwhile, the lowest depth of cut predicted by the FRF with the drawbar (1.138 mm) at 19,710 rpm differed from the depth of cut predicted based on the measured FRF by only 3%. Moreover, the right-hand side of Fig. 15 shows that the SLD predicted based on the FRF with the drawbar was better than the SLD predicted by the FRF without the drawbar at high spindle speeds (35,000 to 120,000 rpm).

We validated our calculations by investigating the effects of tool length on the NF of the spindle, as shown in Fig. 16. As expected, as the tool length varied, the third NF or tool natural frequency varied most, even when the conditions of the drawbar were varied. In this case, the minus sign "-" in "-10 mm" indicates that the current drawbar length was reduced by 10 mm and vice versa. The length of the last portion of the drawbar shown in Fig. 2 was varied between −10 mm and 40 mm in increments of 10 mm. This component was included in the spindle

Table 1
Value of the contact parameter $[K_{3\_2}]$ under different clamping conditions.

F_z(N)	k_{xf}	c_{xf}	k_{xm}	c_{xm}	$k_{\theta f}$	$c_{\theta f}$	$k_{\theta m}$	$c_{\theta m}$
	N/m	Ns/m	Nm/m	Nms/m	N/rad	Ns/rad	Nm/rad	Nms/rad
3.75×10^3	1.33×10^7	2.60×10^4	2.63×10^6	9.01×10^2	6.55×10^6	1.32×10^2	2.66×10^5	0.40×10^0
2.56×10^3	1.04×10^7	9.64×10^3	4.05×10^4	2.35×10^2	1.26×10^7	8.30×10^1	2.95×10^5	0.23×10^0
1.17×10^3	0.94×10^7	7.28×10^3	4.05×10^4	1.88×10^2	1.56×10^7	8.30×10^1	3.98×10^5	0.23×10^0

Table 2
Aerostatic bearing dynamics at different air pressures.

		$[K_{a1}] = [K_{a2}]$			$[K_{a3}] = [K_{a4}]$		
		0.4 MPa	0.5 MPa	0.6 MPa	0.4 MPa	0.5 MPa	0.6 MPa
k_{xf}	(N/m)	16.8×10^6	18×10^6	19.2×10^6	15.9×10^6	16×10^6	16.4×10^6
c_{xf}	(Ns/m)	4.51×10^2	8.31×10^2	1.18×10^3	1.26×10^4	1.03×10^4	1.08×10^4
k_{xm}	(Nm/m)	2.08×10^5	2.81×10^5	2.74×10^5	2.95×10^6	4.37×10^4	2.31×10^4
c_{xm}	(Nms/m)	2.80×10^1	2.59×10^1	5.09×10^1	3.54×10^3	3.37×10^3	4.67×10^3
$k_{\theta f}$	(N/rad)	3.48×10^2	2.14×10^1	2.08×10^1	1.29×10^6	1.89×10^4	5.85×10^4
$c_{\theta f}$	(Ns/rad)	1.71×10^1	5.04×10^1	6.13×10^1	3.34×10^4	3.47×10^4	2.72×10^4
$k_{\theta m}$	(Nm/rad)	5.67×10^4	7.71×10^4	8.12×10^4	3.11×10^7	3.40×10^7	3.40×10^7
$c_{\theta m}$	(Nms/rad)	4.56×10^0	3.81×10^0	4.01×10^0	8.04×10^3	9.87×10^3	1.02×10^4

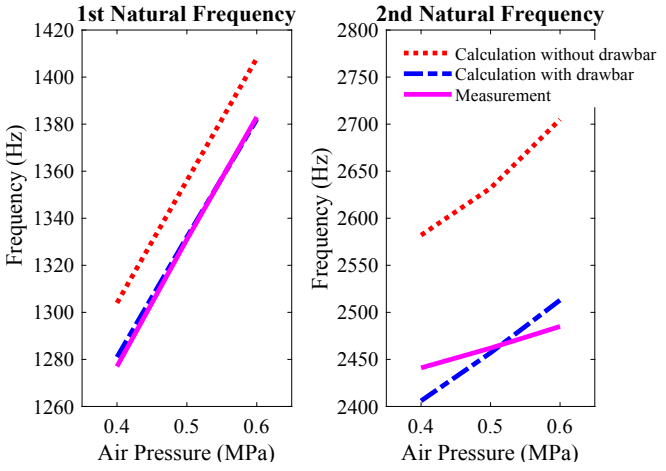

Fig. 12. Comparison between the results of the tool holder B's NF calculation (without and with drawbar) and measurement against the frequency while varying the air pressure.

system using the rigid RCSA method, as mentioned in Appendix B, using Equations (18)–(21).

3.4. Effects of the drawbar on the tool point FRF

From the previous section, we can conclude that the RCSA method provides good estimates of the tool point FRF when the drawbar and values of the contact parameters are taken into account. We can also investigate the effect of the drawbar on the tool point FRF. We investigated the effects of varying two of the properties of the drawbar, namely its length and density.

First, we varied the length of the drawbar in the range [-10 mm–40 mm] in increments of 10 mm. The minus sign "-" in "-10 mm" indicates that the length of the drawbar was reduced by 10 mm and vice versa. The length of the shaft was held constant during this investigation. The effect of varying the length of the drawbar on the tool point NF of the aerostatic bearing spindle is shown in Fig. 17. Fig. 17 is the same as Fig. 16 but zoomed out. The scales on the two sides of the figures are similar. The effects of varying the length of the drawbar are clear visually in the cases of the second and third NFs, but not in the case of the first NF. The calculation is described in Appendix

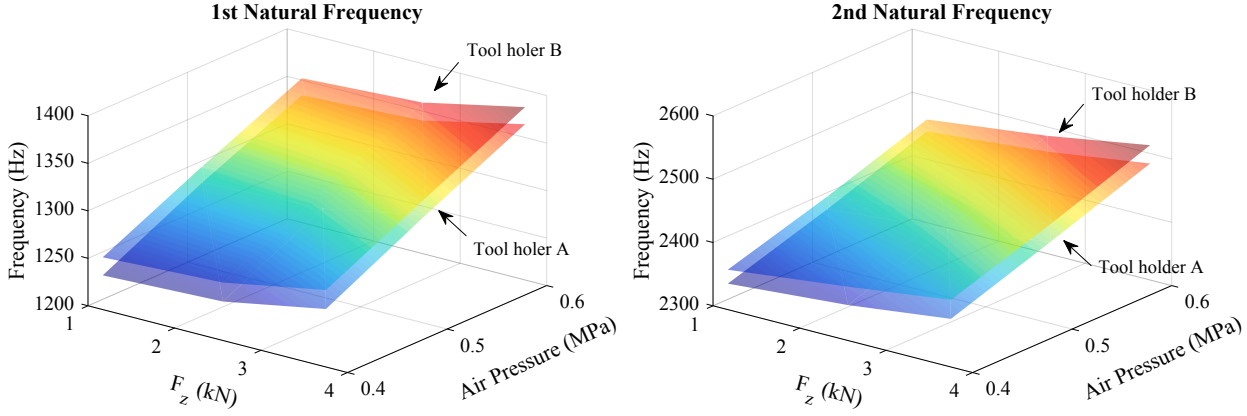

Fig. 13. Difference between tool holder A and tool holder B with respect to the NF, while varying the clamping force F_z and the air pressure (left: 1st NF, right: 2nd NF).

Table 3
Contact parameter of $[K_{2\_1}]$ in different tool holder shank length d_s.

d_s (mm)	k_{xf}	c_{xf}	k_{xm}	c_{xm}	$k_{\theta f}$	$c_{\theta f}$	$k_{\theta m}$	$c_{\theta m}$
	N/m	Ns/m	Nm/m	Nms/m	N/rad	Ns/rad	Nm/rad	Nms/rad
27.5	6.95×10^6	1.38×10^1	1.52×10^5	0.29×10^0	1.52×10^5	0.29×10^0	2.33×10^3	0.07×10^{-1}
24	3.71×10^6	1.69×10^1	9.62×10^4	0.35×10^0	9.62×10^4	0.35×10^0	1.14×10^3	0.13×10^{-1}
17.5	3.03×10^6	2.20×10^1	9.04×10^4	0.26×10^0	9.04×10^4	0.26×10^0	1.31×10^2	0.06×10^{-1}

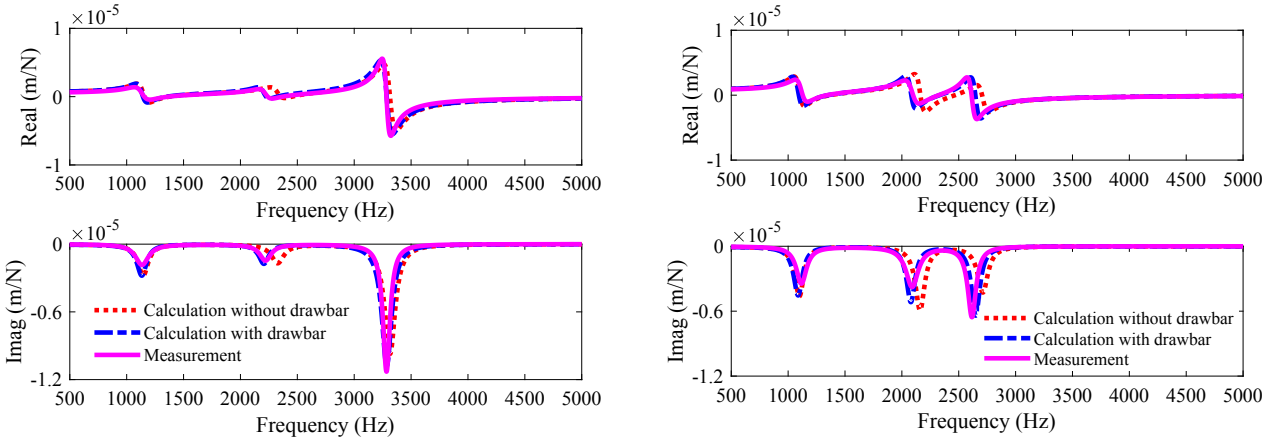

Fig. 14. Comparison between the calculation with and without the drawbar and measurement of the tool point FRF (left: 32.5 mm tool blank, right: 42.5 mm tool blank).

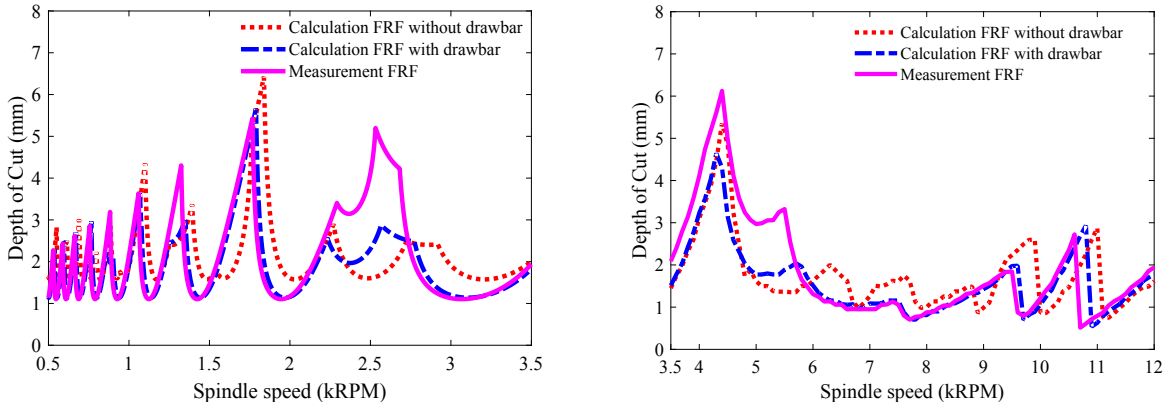

Fig. 15. Comparison between the results of the calculation without and with the drawbar and measurements over the stability lobe diagram at low spindle speeds (left) and high spindle speeds (right).

B, for which we used Equations (18)–(21). In the case of the tool with a length of 32.5 mm, the differences between the NFs of drawbars with length deviations of −10 mm and 40 mm were {4, 129, and 55} Hz for the first, second, and third NF, respectively. In the case of the tool with a length of 42.5 mm, the differences between the NFs of drawbars with length deviations of −10 mm and 40 mm were {5, 71, and 115} Hz for the first, second, and third NF, respectively. Thus, we can conclude that the length of the drawbar does not affect the first NF but does affect the second and third NFs. It is worth noting this phenomenon when designing spindles (as shown in Fig. 18).

We also investigated the effect of the density of the drawbar. We labeled the density variations [0.5x, 1x, 2x, 3x], which indicate half, one time, two times, and three times the initial density. The density of the shaft remained the same. In the case of the tool with a length of 32.5 mm, the differences between the NFs in the cases of 0.5x density

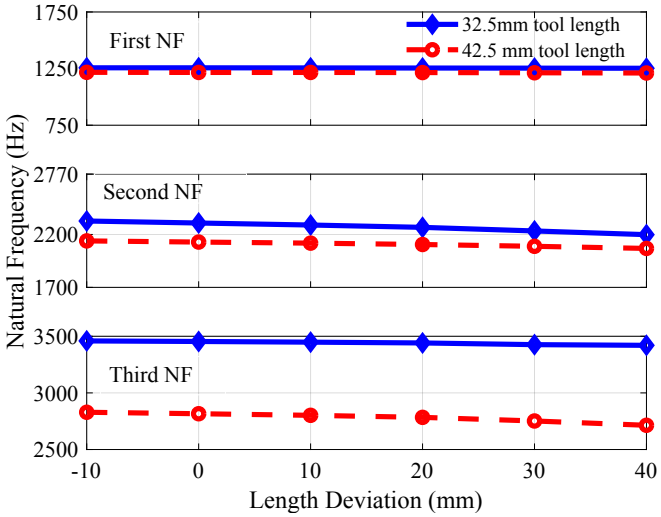

Fig. 16. Effects of tool length on the natural frequency of the tool point. of the aerostatic bearing spindle.

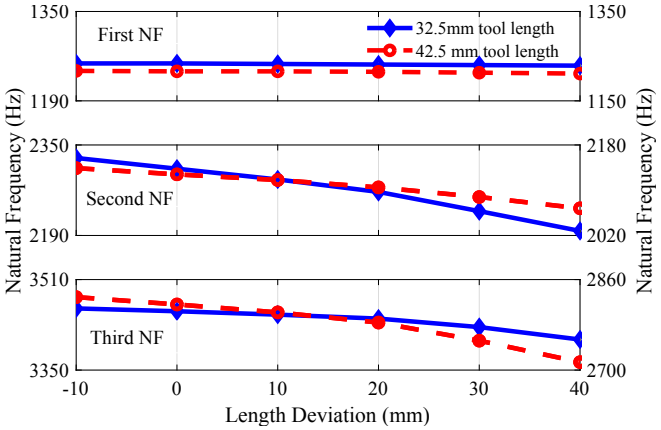

Fig. 17. Effects of the length of the drawbar on the natural frequencies of the aerostatic bearing spindle.

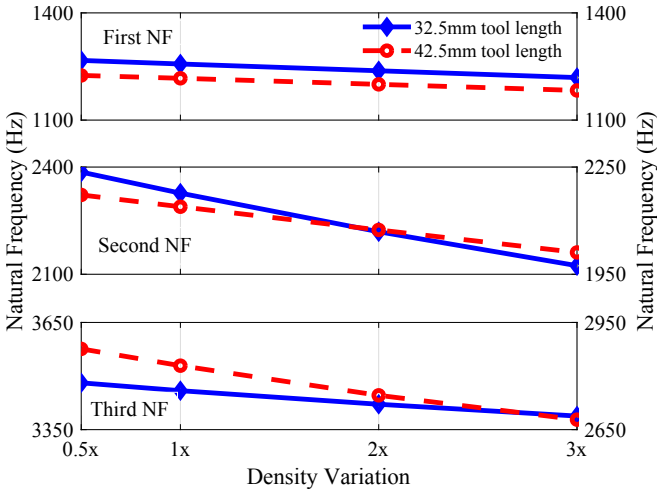

Fig. 18. Effects of the density of the drawbar on the natural frequencies of the aerostatic bearing spindle.

and 3x density were {48, 262, and 93} Hz for first, second, and third NF, respectively. In the case of the tool with a length of 42.5 mm, the differences between the NFs in the cases of 0.5x density and 3x density were {42, 161, and 198} Hz for first, second, and third NF, respectively. Thus, we can conclude that the effect of the density of the drawbar was more pronounced in the case of the second and third NF than the first NF.

4. Conclusion

In this paper, we presented a novel method for predicting the tool point FRF of a multipurpose aerostatic spindle. By including the drawbar, we obtained better estimates of the tool point FRF. We coupled the tool holder to the shaft and confirmed that the FRF at the end point of tool holder was predicted accurately, with a natural frequency (NF) error of 0.4%. We also coupled the tool to the tool holder and the shaft and obtained results that were in good agreement with the measured tool mode frequency data, with a percentage error of 1.7%. This is the first time that two contact parameters, namely those between the shaft and the tool holder and the tool holder and the tool, have been included simultaneously in a tool point FRF calculation. Therefore, this method is suitable for use by spindle designers when they are investigating the properties of spindles prior to production. This method corrects the NF of the shaft-tool holder system before coupling it to the tool by using a better estimate of the contact parameter between the shaft and tool holder; hence, for the tool point FRF, the tool mode frequency is expressed appropriately after coupling an arbitrary tool to the shaft-tool holder system. Furthermore, our method corrects the receptance at frequencies of different modes; we also took into account the dynamics of the aerostatic bearings in the tool point receptance calculation. Thus, our calculation provided a good estimate of the tool point FRF of the spindle. We also estimated the SLD, emphasizing the importance of the inclusion of the drawbar when estimating the spindle dynamics. We also investigated the effect of the length and density of the drawbar and found that, although these do not affect the first NF of the spindle, they do affect the second, and especially the third NF. This information will be important to researchers studying machining. Therefore, it is beneficial to include the drawbar during the optimization stage of the design process.

Acknowledgements

This research was supported by the project titled, “Development of Technology for Mobile Platform-based Machining System” in research programs of Korean Institute of Machinery and Maerials.

Appendix A. RCSA background

RCSA is applied for predicting the receptance of assembly by mathematical combination the receptance of components. In simple case, the receptance is the ratio of transverse deflection to force. In advanced case, the receptance is the ratio of transverse deflection x and rotation about beam axisθ to force f and bending couples m [18].

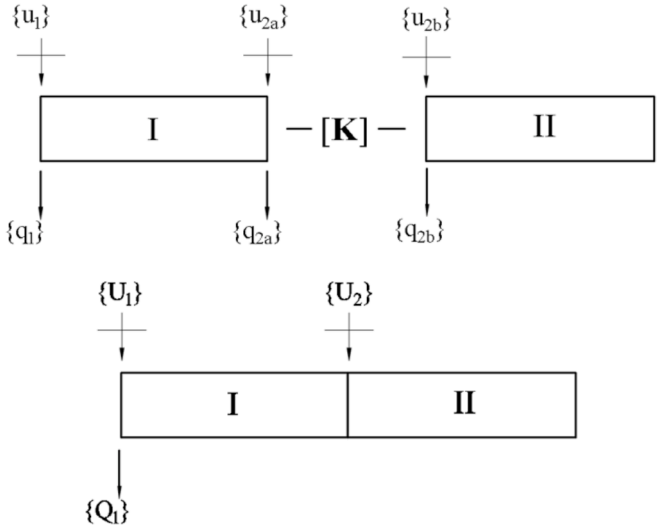

Fig. 19. RCSA model for predicting assembly receptance G_{11}. In case of rigid assembly, [K] is considered to be infinite and [K]-1 = 0,.

The coupling process of tool holder to drawbar-shaft combination or the coupling process of tool to tool holder-drawbar-shaft combination could be model as an example of RCSA display in Fig. 19. In this example, component receptanceR_{11}, and assembly receptance, G_{22}, at point 2 are added. From equilibrium condition $q_{2a} + q_{2b} = 0$and $q_1 = Q_1$ as well as compatibility condition$[K]\{u_{2b} - u_{2a}\} = -[q_{2b}]$, the assembly receptance, G_{11}, at point 1 could be express as Eq. (17):

$$[G_{11}] = [R_{11}] - [R_{12a}]([R_{2a2a}] + [R_{2b2b}] + [K]^{-1})^{-1}[R_{2a1}] \tag{17}$$

$$[G_{11}] = [R_{11}] - [R_{12a}]([R_{2a2a}] + [R_{2b2b}])^{-1}[R_{2a1}] \tag{18}$$

$$[G_{21}] = [R_{2a1}] - [R_{2a2a}]([R_{2a2a}] + [R_{2b2b}])^{-1}[R_{2a1}] \tag{19}$$

$$[G_{12}] = [R_{12a}] - [R_{12a}]([R_{2a2a}] + [R_{2b2b}])^{-1}[R_{2a2a}] \tag{20}$$

$$[G_{22}] = [R_{2a2a}] - [R_{2a2a}]([R_{2a2a}] + [R_{2b2b}])^{-1}[R_{2a2a}] \tag{21}$$

Appendix B. Multiple-point receptance coupling approach

In order to predict the FRF of shaft drawbar assembly, four-point receptance coupling is used as described in Ref. [16]. Based on four contacting points of shaft and drawbar, the assembly is devided to three segments as in Fig. 20. U_1 and Q_1 are the corresponding generalized displacement/rotation and external force/moment vectors acting on the shaft drawbar assembly.

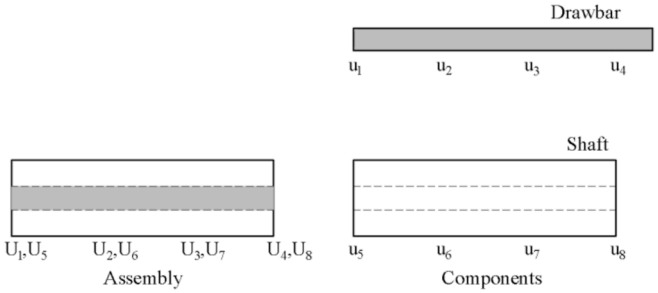

Fig. 20. Shaft drawbar assembly and components..

In Eq. (1), q_j/Q_1 (j = 1 … 4) is obtain from matrix [A] where the two rows in order j of [A] is equal to q_j/Q_1. Generally, [A] has the form in Eq. (22) where n is coupling points.

$$[A] = \begin{bmatrix} R_{11} + R_{n+1,n+1} & R_{12} + R_{n+1,n+2} & \cdots & R_{1n} + R_{n+1,n+n} \\ R_{21} + R_{n+2,n+1} & R_{22} + R_{n+2,n+2} & \cdots & R_{2n} + R_{n+2,n+n} \\ \vdots & \vdots & \ddots & \vdots \\ R_{n1} + R_{n+n,n+1} & R_{n2} + R_{n+n,n+n} & & R_{nn} + R_{n+n,n+n} \end{bmatrix}^{-1} \begin{bmatrix} R_{n+1,n+1} \\ R_{n+2,n+1} \\ \vdots \\ R_{n+n,n+1} \end{bmatrix} \tag{22}$$

In this paper, n is equal to 4; therefore, Eq. (22) is derived to Eq. (23).

$$[A] = \begin{bmatrix} R_{11} + R_{55} & R_{12} + R_{56} & R_{13} + R_{57} & R_{14} + R_{58} \\ R_{21} + R_{65} & R_{22} + R_{66} & R_{23} + R_{67} & R_{24} + R_{68} \\ R_{31} + R_{75} & R_{33} + R_{76} & R_{33} + R_{77} & R_{34} + R_{78} \\ R_{41} + R_{85} & R_{42} + R_{86} & R_{43} + R_{87} & R_{44} + R_{88} \end{bmatrix}^{-1} \begin{bmatrix} R_{55} \\ R_{65} \\ R_{75} \\ R_{85} \end{bmatrix} \tag{23}$$

The drawbar receptance matrix contain $4^2 = 16$ terms R_{ij}. Nevertheless, due to reciprocity, the term of R_{ij} needed to be determined is placed on the upper triangular portion of R_{ij} matrix, i.e. $\sum_{i=1}^{4} i = 10$ terms. The ten terms of upper triangular portion of R_{ij} is determined based on RCSA method which is described as followed.

The three corners of the upper triangular including R_{11},R_{14},R_{44} are identified by Timoshenko beam theory.

The two remaining terms in the first row the R_{ij} matrix, i.e. R_{1j} where j = 2 to n – 1, or R_{12}, R_{13} are identified by Eq. (24):

$$R_{1j} = E_{1ja}(E_{jaja} + E_{jbjb})E_{jbjb} \tag{24}$$

where ja and jb represents for two points of two segments when the shaft is virtually separated at coupling point j. In case of i and j are equal, E_{ij} is direct receptance of the separated beam at the coupling point i, in case of i and j are not equal, E_{ij} is the cross receptance of the separated beam have length from coupling point i to coupling point j.

The two remaining terms in the last column of the R_{ij} matrix, i.e. R_{in} where i = 2 to n – 1, or R_{24}, R_{34} are identified by Eq. (25):

$$R_{i4} = E_{iaia}(E_{iaia} + E_{ibib})E_{ib4} \tag{25}$$

where E_{ij} is modeled using Timoshenko beam similarly with method mentioned above.

The two remaining terms in the diagonal of the R_{ij} matrix, i.e. R_{ii} where i = 2 to n – 1, or R_{22}, R_{33} are identified by Eq. (26):

$$R_{ii} = E_{iaia}(E_{iaia} + E_{ibib})E_{ibib} \tag{26}$$

where E_{iaia} is direct receptance of left segments at the right end, and E_{ibib}, the direct receptance of right segment at the left end are identified by Timoshenko beam theory as described previously.

The last remaining team above the diagonal of R_{ij} matrix, excluding the last column and the first row, i.e. R_{23} is identified by Eq. (27):

$$R_{23} = E_{23a}(E_{3a3a} + E_{3b3b})E_{3b3b} \tag{27}$$

where E_{3a3a} and E_{3b3b} are direct receptance of left segment and right segment at right end and left end, respectively. The receptance E_{23a} of left end segment is calculated using RCSA. The left end segment is divided to two smaller segments at coupling point n = 2, E_{23a} could be identified by Eq. (28):

$$E_{23a} = S_{2a2a}(S_{2a2a} + S_{2b2b})S_{2b3a} \quad (28)$$

where S_{2a2a} and S_{2b2b} are the direct receptance of left smaller segment and right smaller segment at right end and left end, respectively; and S_{2b3a} is the cross receptance of smaller segment from coupling node 2 and coupling node 3. These receptances are identified by Timoshenko beam theory.

The drawbar has a small segment at right side of coupling node 4. The effect of this segment to the R_{ij} matrix could be shown by rigid RCSA from Eq. (18) to Eq. (21). Component II and component I in Fig. (20) represent for small drawbar segment at right end and shaft segment R_{ij} when j = 4, respectively.

The upper triangular terms of matrix R_{ij} have been determined. The full R_{ij} matrix could be obtained by symmetry characteristic.

The shaft receptance matrix is identified in the same manner mentioned above with exception that the shaft does not have the small segment at right end of itself; therefore adding small segment at coupling node 4 is omitted. The coordinate is changed to shaft coordinated from n + 1 to 2n, or 5 to 8. Additionally, shaft geometry and material characteristic is updated.

The English in this document has been checked by at least two professional editors, both native speakers of English. For a certificate, please see:http://www.textcheck.com/certificate/szNqMo.

References

[1] H. Schulz, T. Moriwaki, High-speed machining, CIRP Ann. - Manuf. Technol. 41 (1992) 637–643, https://doi.org/10.1016/S0007-8506(07)63250-8.

[2] W. Tobias, S.A. Fishwick, Theory of Regenerative Machine Tool Chatter, Engineer, (1958), p. 205.

[3] J. Tlusty, Manufacturing Processes and Equipment, Prentice Hall, Upper Saddle River, NJ, 2000.

[4] E. Budak, Y. Altintaş, Analytical prediction of chatter stability in milling—Part I: general formulation, J. Dyn. Syst. Meas. Control 120 (1998) 22–30, https://doi.org/10.1115/1.2801317.

[5] E. Budak, Y. Altintas, Analytical prediction of chatter stability in milling - Part II: application of the general formulation to common milling systems, J. Dyn. Syst. Meas. Control. Asme. 120 (1998) 31–36, https://doi.org/10.1115/1.2801318.

[6] S. Jiang, S. Zheng, A modeling approach for analysis and improvement of spindle-drawbar-bearing assembly dynamics, Int. J. Mach. Tool Manuf. 50 (2010) 131–142, https://doi.org/10.1016/j.ijmachtools.2009.08.010.

[7] J. Hung, Y. Lai, T. Luo, K. Wu, Y. Zhan, Effect of Drawbar Force on the Dynamic Characteristics of a Spindle-Tool Holder System vol. 8, (2014), pp. 1022–1027.

[8] S. Jiang, S. Zheng, Dynamic design of a high-speed motorized spindle-bearing system, J. Mech. Des. 132 (2010) 34501, https://doi.org/10.1115/1.4001109.

[9] O. Özşahin, A. Ertürk, H.N. Özgüven, E. Budak, A closed-form approach for identification of dynamical contact parameters in spindle-holder-tool assemblies, Int. J. Mach. Tool Manuf. 49 (2009) 25–35, https://doi.org/10.1016/j.ijmachtools.2008.08.007.

[10] T.L. Schmitz, M.A. Davies, M.D. Kennedy, Tool point frequency response prediction for high-speed machining by RCSA, J. Manuf. Sci. Eng. 123 (2001) 700, https://doi.org/10.1115/1.1392994.

[11] T.L. Schmitz, Predicting high-speed machining dynamics by substructure analysis, CIRP Ann. - Manuf. Technol. 49 (2000) 303–308, https://doi.org/10.1016/S0007-8506(07)62951-5.

[12] J.C.Z. Schmitz, L. Tony, Kevin Powell, Dongki Won, G. Scott Duncan, W. Gregory Sawyer, Shrink fit tool holder connection stiffness/damping modeling for frequency response prediction in milling, Int. J. Mach. Tool Manuf. 47 (2007) 1368–1380.

[13] A. Ertürk, H.N. Özgüven, E. Budak, Analytical modeling of spindle-tool dynamics on machine tools using Timoshenko beam model and receptance coupling for the prediction of tool point FRF, Int. J. Mach. Tool Manuf. 46 (2006) 1901–1912, https://doi.org/10.1016/j.ijmachtools.2006.01.032.

[14] M. Postel, O. Özsahin, Y. Altintas, High speed tooltip FRF predictions of arbitrary tool-holder combinations based on operational spindle identification, Int. J. Mach. Tool Manuf. (2018), https://doi.org/10.1016/j.ijmachtools.2018.03.004.

[15] Y. Ji, Q. Bi, S. Zhang, Y. Wang, A new receptance coupling substructure analysis methodology to predict tool tip dynamics, Int. J. Mach. Tool Manuf. (2018), https://doi.org/10.1016/j.ijmachtools.2017.12.002.

[16] T.L. Schmitz, G.S. Duncan, Receptance coupling for dynamics prediction of assemblies with coincident neutral axes, J. Sound Vib. 289 (2006) 1045–1065, https://doi.org/10.1016/j.jsv.2005.03.006.

[17] S.S. Park, Y. Altintas, M. Movahhedy, Receptance coupling for end mills, Int. J. Mach. Tool Manuf. 43 (2003) 889–896, https://doi.org/10.1016/S0890-6955(03)00088-9.

[18] T.L. Schmitz, K.S. Smith, Mech. Vib. (2012), https://doi.org/10.1007/978-1-4614-0460-6.

[19] R.D. Blevin, Formulas for Natural Frequency and Mode Shape, Krieger, Malabar, 1979.

[20] U.V. Kumar, T.L. Schmitz, Spindle dynamics identification for receptance coupling substructure analysis, Precis. Eng. 36 (2012) 435–443, https://doi.org/10.1016/j.precisioneng.2012.01.007.

[21] T.L. Schmitz, K.S. Smith, Machining Dynamics, Springer, Boston, MA, 2009, https://doi.org/10.1007/978-0-387-09645-2_1.